DOI 10.1007/s11182-021-02473-5
Russian Physics Journal, Vol. 64, No. 8, December, 2021 (Russian Original No. 8, August, 2021)

HEAT INPUT EFFECT ON THE STRUCTURE OF ZhS6U ALLOY PRODUCTS PRODUCED BY WIRE-FEED ELECTRON-BEAM ADDITIVE MANUFACTURING

D. A. Gurianov, S. V. Fortuna, S. Yu. Nikonov, E. N. Moskvichev, and E. A. Kolubaev

UDC 620.184.3

The paper studies the process conditions of wire-feed electron beam additive manufacturing (EBAM) that change the structure of the samples obtained. It is shown that the EBAM process can produce defect-free samples with a directed structure. The structure of the EBAM-produced samples is investigated and the difference between the initial and the obtained material is identified. The heat input effect on the structural stability of the alloy samples is determined together with the main parameter, namely the primary dendrite arm spacing. It is found that the dynamic change in the electron beam current retards the increase in the primary dendrite arm spacing. The obtained values of this parameter indicate to the achievement of the temperature gradients required for the structure formation with direct orientation.

Keywords: additive manufacturing, heat-resistant alloys, microstructure, grain orientation.

INTRODUCTION

Heat-resistant nickel- and cobalt-based alloys and steels are often used in the production of hot section components of gas-turbine engines and plants. These alloys possess high strength, resistance to high-temperature creep and corrosion [1–3]. The single crystal or directed structure must be formed during the manufacturing products operating in extreme conditions, [3]. The products having such a structure are currently obtained by the Bridgman–Stockbarger technique, which includes a slow motion of a crystallizing workpiece from the heating to cooling zone. Since this approach implies cooling due to the radiation-induced heat sinking, the temperature gradient is rather low (10–20°C/cm) near the crystallization front. This technique is developed as a grain orientation process using a liquid metal coolant. The difference between this technique and the Bridgman–Stockbarger technique is that the cooling zone is a low-melt material such as aluminum or tin. The new technique allows increasing the temperature gradient up to 200°C/cm [4]. This increase is conditioned by the possibility of reducing the dendrite size (primary dendrite arm spacing), porosity, and dendritic segregation [5].

In recent years, the additive manufacturing has dominated other production techniques [6]. Several approaches to the production of workpieces from pure metals and alloys have been developed. For example, electron or laser beams can serve as a heating source as well as an electric arc. The feed material such as powder, wire, or powder bed fusion can be utilized to fabricate a product [6]. Additive manufacturing reduces the use of waste materials, simplifies the fabrication of shaped products, and combines different initial materials due to series or parallel feed of filaments. This technique involves local melting and crystallization resulting in the growth of the temperature gradient and cooling rate. Several works are devoted to the manufacture of products with a directed or single-crystal structure [7]. One of the

Institute of Strength Physics and Materials Science of the Siberian Branch of the Russian Academy of Sciences, Tomsk, Russia, e-mail: desa-93@mail.ru; s_fortuna@ispms.tsc.ru; SergRFF@ngs.ru; em_tsu@mail.ru; eak@ispms.ru.
Translated from Izvestiya Vysshikh Uchebnykh Zavedenii, Fizika, No. 8, pp. 31–37, August, 2021. Original article submitted February 15, 2021.

TABLE 1. Grade Chemical Composition of ZhS6U Alloy, wt.% [9]

Cr	C	Al	Ti	W	Nb	Co	Fe
8.0–9.5	0.13–0.2	5.1–6.0	2.0–2.9	9.5–11.0	0.8–1.2	9.0–10.5	≤1
Mo	Ni	Residues (Si, S, Mn, P, Ce, Zr, B, Pb, Bi, Y)					
1.2–2.4	Base	up to 0.93					

TABLE 2. Process Conditions of Additive Manufacturing

Samples	Acceleration voltage, kV	Displacement rate of table, mm/min	Beam current, mA
1	30	20	First layer: 28 Last layer: 16
2	30	20	First layer: 25 Last layer: 10

applications of the grain orientation in additive manufacturing is healing of defects in products obtained by conventional casting. Another includes the fabrication of new products using single-crystal substrates. After a completion of the additive manufacturing process, the substrate must be removed, and such a technique significantly increases the production cost. In this connection, it is interesting to achieve the grain orientation in the manufacturing process using substrates made of more available materials.

MATERIALS AND METHODS

The alloy samples were obtained by wire-feed electron-beam additive manufacturing (EBAM) on an equipment developed at the Institute of Strength Physics and Materials Science SB RAS, Tomsk, Russia [8]. The rods were made of the ZhS6U (namely K465 or M963) cast alloy, whose grade chemical composition is given in Table 1.

This alloy relates to heat-resistant alloys of the first generation, which was intended for the production of aircraft engine parts with an equiaxial structure. But according to previous research [10, 11], additive manufacturing allowed gaining a directed structure of heat-resistant alloy samples of the first and second generations. In our research [10], additive manufacturing of samples was conducted on an austenite steel, in vacuum conditions. The heat-resistant alloy rods were fed to the electron beam for melting. During the table displacement, the rod feeding system provided the layer-by-layer formation of the thin-walled samples. The main conditions of the EBAM process included the acceleration voltage and the displacement rate of the table, that did not change during 3D printing of one sample. The beam current monotonically reduced with increasing sample height due to the necessity of decreasing the heat input [12] in the consequence of the lower heat sinking. It should be noted that in fabricating Sample 2, we used a dynamic change in the electron beam current. It meant that at the beginning and end of each layer formation, the beam current reduced by 1–2 mA as compared to the layer centre. The EBAM-produced samples consisted of 20 layers and were 4.19 cm (Sample 1) and 4.53 cm (Sample 2) high. The process conditions are presented in Table 2.

The specimens cut from the EBAM-produced samples were used to study their macro and microstructure, chemical and phase compositions by using optical and scanning electron microscopies (SEM). The temperature gradient was identified by measuring the primary dendrite arm spacing. After abrasion and polishing, the samples underwent marble etching in 20 mL HCl, 5 g $CuSO_4 \cdot 5H_2O$ and 80 mL H_2O, and then were studied on an optical microscope. An Oxford Instruments Ultim Max 40 energy dispersive X-ray spectroscopy (EDS) on the scanning electron microscopes Zeiss EVO 50 (Germany) and MIRA 3 LMU (Tescan, Czech) was carried out to investigate the fine structure and the real chemical composition of the structural elements.

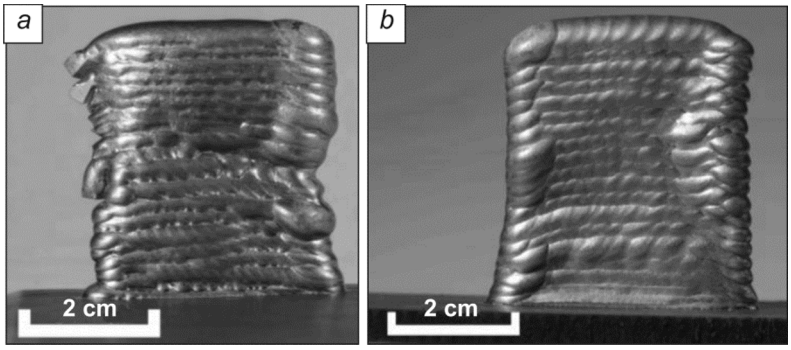

Fig. 1. Wire-feed EBAM samples produced from heat-resistant ZhS6U alloy: *a* – Sample 1, *b* – Sample 2.

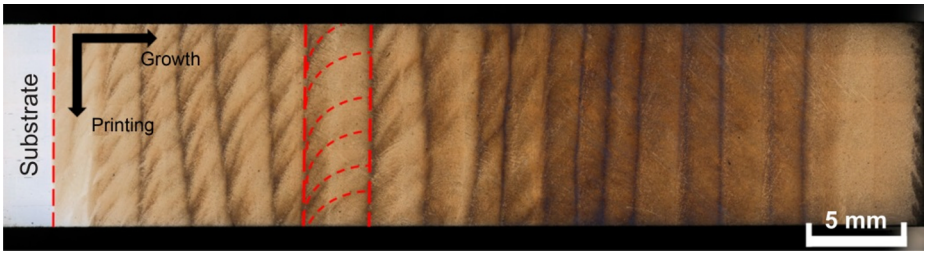

Fig. 2. Macrostructure of EBAM-produced Sample 2 made of ZhS6U alloy. Arrows indicate the directions of manufacturing growth and printing.

RESULTS AND DISCUSSION

The photographs of the EBAM-produced samples are presented in Fig. 1. These samples have the form of walls; they have no macro-defects such as cracks, unmolten or laminated regions. Sample 1 demonstrates the shape defects.

The main EBAM process conditions – acceleration voltage (U, kV), beam current (I, mA) and displacement rate of the table (v, mm/min) can be expressed through the heat input (Q, kJ/mm) [13]:

$$Q = \frac{60 \times U \times I}{1000 \times v}. \quad (1)$$

Taking Eq. (1) and the data from Table 2 into consideration, the heat input changes with increasing height from 2.79 to 1.08 kJ/mm for Sample 1 and from 2.25 to 0.90 kJ/mm for Sample 2. The samples are manufactured by using unidirectional printing, i.e., layer by layer, in one direction. In all, 20 layers are produced, but the decrease in the heat input (in the case of Sample 2) results in a smaller deviation from the specified geometry and the higher wall of the sample.

Figure 2 presents the cross-sectional view of the macrostructure of Sample 2. One can see dendrite colonies epitaxially growing through the layers, in the direction of the additive manufacturing growth. At the same time, there is an inclination in the direction of the layer printing.

In our previous research [10] we show that the inclination of the dendrite colonies toward the layer printing occurs due to a distortion of the crystallization front. In turn, the concave crystallization front results from its rather

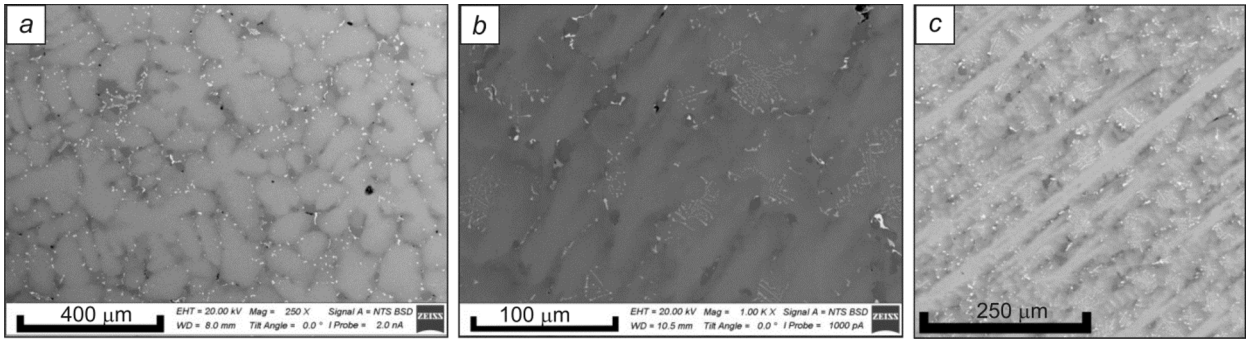

Fig. 3. Macrostructure of ZhS6U alloy in the initial state (*a*) and EBAM-produced samples: *b* – Sample 1, *c* – Sample 2.

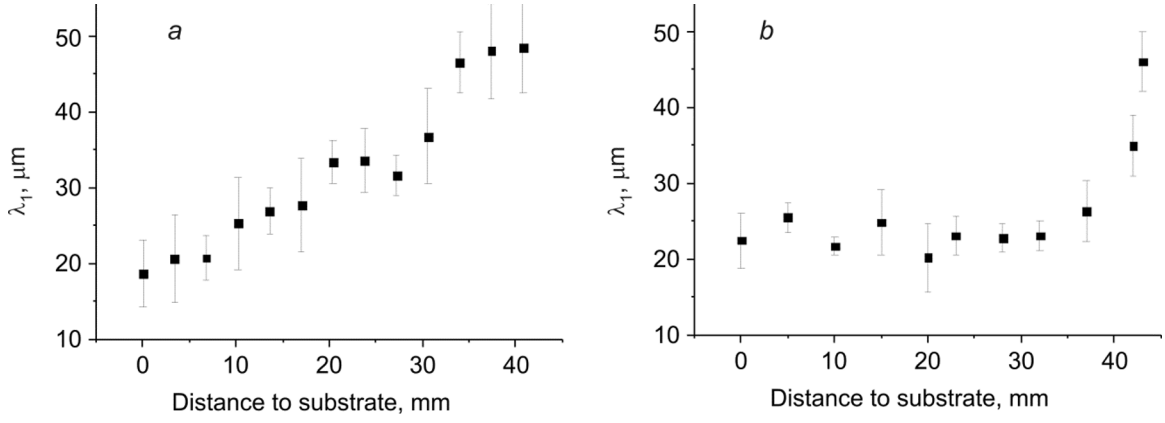

Fig. 4. Dependences between average primary dendrite arm spacing and distance to the substrate: *a* – Sample 1, *b* – Sample 2.

rapid movement during the printing process. The structure of the EBAM-produced samples is characterized by distinct layer boundaries and molten pools schematically depicted in Fig. 2 by dashed straight and curved lines, respectively.

As presented in Fig. 3, the microstructure of the EBAM-produced samples is characterized by a smaller size of dendrites and secondary phases as compared to the initial alloy state, and also by a single direction of the additive manufacturing growth of the primary dendrite arm spacing and significant reduction of secondary arms. At the substrate boundary (in the maximum temperature gradient), dendrites are thinner, without secondary arms. These changes are caused by a localized crystallization process observed in additive manufacturing. This, in turn, leads to an increase in the temperature gradient at the crystallization front and, consequently, an increase in the cooling rate. It is worth noting that the dendrite growth is more directed in Sample 2.

Bondarenko and Kablov [5] find the primary dendrite arm spacing (λ_1, μm) to be a convenient structural property of the material of products with the directed structure. When $\lambda_1 \approx 200$ μm, in Sample 1 it changes from 18.7 μm near the substrate to 48.4 μm near the upper end of the sample. In the case of Sample 2, these values change from 22.5 to 46.0 μm. The dependences between the primary dendrite arm spacing and the distance to the substrate are shown in Fig. 4. One can see that in the case of Sample 1, the λ_1 value monotonically grows, whereas for Sample 2, it grows significantly in two last layers only. The difference in the primary dendrite arm spacing is probably associated with the values of the reduced heat input and the dynamic change in the electron beam current in the case of Sample 2. The growth in the λ_1 value with increasing distance to the substrate (sample height) depends on the reduced heat sinking to the substrate *via* the thermal conductivity and increasing radiation component of the heat dissipation. This is described in detail in [10].

TABLE 3. Chemical Composition of Structural Elements of cast ZhS6U Alloy and EBAM-Produced Samples, wt.%

Materials	Structural elements	Al	Ti	Cr	Co	Ni	Nb	Mo	W
Initial	Dendrites	12.50	2.14	9.91	10.42	59.87	0.24	0.99	3.83
	Interdendritic space	13.17	3.49	11.28	9.44	58.65	0.53	1.34	2.13
	MC carbides	0.82	54.49	1.55	0.62	4.32	17.74	3.31	17.28
	M_6C carbides	1.45	3.78	35.89	3.25	10.36	4.10	22.72	18.42
Sample 1	Dendrites	11.84	2.44	10.59	10.32	60.39	–	1.04	3.91
	Interdendritic space	12.29	3.53	10.09	9.73	61.07	–	0.98	2.96
	MC carbides	–	42.89	4.07	1.86	11.24	21.21	–	18.76
	M_6C carbides	2.92	4.43	24.23	5.82	27.96	–	13.75	20.89
Sample 2	Dendrites	11.26	1.99	9.66	10.74	60.43	0.22	0.96	4.25
	Interdendritic space	11.93	2.67	10.28	10.23	59.64	0.36	1.04	3.44
	MC carbides	1.87	41.89	4.20	2.15	13.33	13.27	4.47	18.66

As was mentioned above, the electron beam current changed within each layer of Sample 2. Additional research was carried out to determine the structural response to these changes. Using optical and scanning electron microscopes, one of the layers was investigated at a 20 mm distance to the substrate. It was found that the primary dendrite arm spacing λ_1 was 27.7 at the beginning of the layer. Then it monotonically decreased to 20.0 μm at the centre and monotonically grew up to 33.0 μm at the end of the layer. In the case of Sample 1, when the beam current was constant during the layer growth, the primary dendrite arm spacing λ_1 monotonically increased from 28.6 μm at the beginning to 37.15 μm at the end of the layer, without a notable decrease at the centre. Apparently, in the case of Sample 2, large λ_1 values at the beginning and end of the layer (nearby the end surfaces of the sample) were provided by the growing contribution of the radiation component of the heat sinking through the free surfaces of the sample.

It is interesting to note that in Sample 2, the volume fraction of the dendrite colonies with large-angle misorientations, is much greater than in Sample 1. Based on the obtained λ_1 values and the microstructure, it can be argued that the formation of the more stable structure occurs within one layer of Sample 1.

The temperature gradients are determined by the dependence of the λ_1 value on the crystallization parameters [14]:

$$\lambda_1 = 134.34(G \cdot R)^{-0.26}, \quad (2)$$

where G is the temperature gradient, °C/cm; R is the crystallization velocity, mm/min.

Equation (2) shows that at a constant crystallization velocity, the λ_1 value is mostly affected by the temperature gradient. With respect to the experimental data and the table displacement velocity, we obtain the values of the temperature gradient during the additive manufacturing process. Thus, with increasing height, the temperature gradient lowers from 577 to 15°C/cm for Sample 1 and from 284 to 18°C/cm for Sample 2. In several works [10, 15, 16], it is shown that either equiaxial structures or strongly misoriented dendrite colonies always appear in the last layers of the EBAM-produced samples. In the case of samples with the directed structure, these regions are usually removed at the final stage of additive manufacturing. Therefore, the structural properties of the last layers of the EBAM-produced samples can be neglected. The optimum primary dendrite arm spacing ranges between 22.5 and 26.3 μm for Sample 2, which matches the temperature gradient range of 284–156°C/cm.

Using the SEM-EDS analysis, the chemical composition is identified for different structural elements of the cast alloy and the EBAM-produced samples. The ZhS6U alloy structure and phase composition include dendrites, interdendritic space, MC carbides (where M is Ti, Nb, W), and M_6C carbides (where M is Cr, Mo, W). The chemical composition obtained in our experiments for ZhS6U structural elements is presented in Table 3.

As can be seen from Table 3, a transition from the cast alloy to additive manufacturing has no effect on the chemical element distribution in the structure and phase composition of the ZhS6U alloy. The same relates to the change in the process conditions of the wire-feed electron-beam additive manufacturing, when comparing Samples 1 and 2, namely the change in the heat input. It should be noted that SEM observations do not show the presence of M_6C carbides in Sample 2 due to their significant refinement. This fact requires further deep investigations of the phase composition.

CONCLUSIONS

The wire-feed electron beam additive manufacturing was used to fabricate samples from heat-resistant nickel alloy. It was found that in the local melting conditions, the structure and phase composition of the EBAM material were highly sensitive to changes in the process conditions.

Despite the control for the heat input reduction during the layer-by-layer printing, the size of the main structural elements monotonically grew in the material of the nickel samples due to the formation of the primary dendrite arm spacing.

It was shown that a combination of the monotonic reduction in the heat input and variation of the beam current during each layer growth led to lower deviations from the specified sample geometry and retardation of the increase in the average primary dendrite arm spacing λ_1 when depositing new layers. Thus, for the sample with the constant beam current in the layers, the λ_1 value ranged from 18.7 to 45.5 μm near the substrate and the upper layers, respectively. When the beam current was changed in each layer, the λ_1 value ranged from 22.5 to 26.3 μm over the sample height, except for the last layers at the top of the samples with the equiaxial structure.

This approach, however, provides a notable increase in the dendrite colonies with large-angle misorientations in each layer structure with a simultaneous heterogeneity increase in the λ_1 value.

The type of the surface microstructure of the EBAM-produced samples was determined by the ratio between the heat sinking from the molten pool to the substrate *via* the preceded layers, due to the thermal conductivity and increasing radiation component of the heat dissipation.

It was shown that the EBAM process could maintain the temperature gradient at 200°C/cm, which met the requirements of the up-to-date approaches to the grain orientation of EBAM products made of heat-resistant nickel alloys. Unlike the cast alloy, no chemical element redistribution was observed in the structure and phase composition of the material of EBAM products made of the ZhS6U alloy.

The work was performed according to the Government research assignment for the Institute of Strength Physics and Materials Science SB RAS, project FWRW-2019-0034. Investigations were carried out using the equipment of the Analytical Center of Geochemistry of Natural Systems of National Research Tomsk State University and Nanotekh Regional Core Facility Centre of the Institute of Strength Physics and Materials Science SB RAS.

REFERENCES

1. P. Fernandez-Zelaia, O. D. Acevedo, and M. M. Kirka, Metall. Mater. Trans. A: Phys. Metall. Mater. Sci., **52,** 574–590 (2021).
2. L. Zhu, Z. Yang, B. Xin, *et al*., Surf. Coat. Technol., **410**, 126964 (2021).
3. G. Liu, D. Du, K. Wang, *et al*., Mat. Sci. Eng. A-Struct., **808**, 140911 (2021).
4. Yu. A Bondarenko, A. B. Echin, V. E. Bazhenov, and A. V. Koltygin, Izv. Vyssh. Uchebn. Zaved., Tsvetnaya metallurgiya, No. 4, 53–61 (2017).
5. Yu. A. Bondarenko and E. N. Kablov, Met. Sci. Heat Treat., No. 7, 288–291 (2002).
6. T. DebRoy, T. Mukherjee, H. L. Wei, *et al*., Nat. Rev. Mater., **4**, 48–68 (2021).
7. S. Ci, J. Liang, J. Li, *et al*., J. Alloys Compd., **854**, 157180 (2021).
8. S. Yu. Tarasov, A. V. Filippov, N. N. Shamarin, *et al*., J. Alloys Compd., **803**, 364–370 (2019).
9. OST 90126-85 Vacuum-Melted High-Temperature Cast Alloys [in Russian].

10. S. V. Fortuna, D. A. Gurianov, K. N. Kalashnikov, *et al*., Metall. Mater. Trans. A: Phys. Metall. Mater. Sci., **52**, No. 2, 857–870 (2021).
11. Liu Zhaoyang and Shu Jiayang, Material, **13**, 2300 (2020).
12. ISO 857-1:2002 Welding and Allied Processes. Vocabulary, Part 1: Metal Welding Processes.
13. S. Yu. Tarasov, A. V. Filippov, N. L. Savchenko, *et al*., Int. J. Adv. Manuf. Tech., **99**, 2353–2363 (2018).
14. Y. Zhang, B. Huang, and J. Li, Metall. Mater. Trans. A: Phys. Metall. Mater. Sci., **44**, 1641–1644 (2013).
15. Z. Zhou, Q. Lei, Z. Yan, *et al*., Mater. Design, **198**, 190296 (2021).
16. K. N. Kalashnikov, A. V. Chumaevskii, T. A. Kalashnikova, K. S. Osipovich, and E. A. Kolubaev, Russ. Phys, J., **63**, No. 6, 962–967 (2020).